Publication Year	2022
Acceptance in OA@INAF	2022-09-27T12:52:20Z
Title	Magnetic field strength in cosmic web filaments
Authors	CARRETTI, ETTORE; VACCA, VALENTINA; O'Sullivan, S. P.; Heald, G. H.; Horellou, C.; et al.
DOI	10.1093/mnras/stac384
Handle	http://hdl.handle.net/20.500.12386/32652
Journal	MONTHLY NOTICES OF THE ROYAL ASTRONOMICAL SOCIETY
Number	512

Monthly Notices of the ROYAL ASTRONOMICAL SOCIETY

MNRAS **512,** 945–959 (2022) https://doi.org/10.1093/mnras/stac384
Advance Access publication 2022 February 14

Magnetic field strength in cosmic web filaments

Ettore Carretti [1]★ V. Vacca [2] S. P. O'Sullivan [3] G. H. Heald [4] C. Horellou,[5] H. J. A. Röttgering,[6] A. M. M. Scaife [7,8] T. W. Shimwell,[6,9] A. Shulevski [6] C. Stuardi [1,10] and T. Vernstrom [4]

[1] INAF Istituto di Radioastronomia, Via Gobetti 101, I-40129 Bologna, Italy
[2] INAF Osservatorio Astronomico di Cagliari, Via della Scienza 5,I- 09047 Selargius (CA), Italy
[3] School of Physical Sciences and Centre for Astrophysics & Relativity, Dublin City University, Glasnevin D09 W6Y4, Ireland
[4] CSIRO, Space and Astronomy, PO Box 1130, Bentley, WA 6102, Australia
[5] Chalmers University of Technology, Department of Space, Earth and Environment, Onsala Space Observatory, SE-43992 Onsala, Sweden
[6] Leiden Observatory, Leiden University, PO Box 9513, NL-2300 RA Leiden, The Netherlands
[7] Jodrell Bank Centre for Astrophysics, Department of Physics & Astronomy, University of Manchester, Manchester M13 9PL, UK
[8] The Alan Turing Institute, 96 Euston Road, London NW1 2DB, UK
[9] ASTRON, Netherlands Institute for Radio Astronomy, Oude Hoogeveensedijk 4, NL-7991 PD Dwingeloo, The Netherlands
[10] Dipartimento di Fisica e Astronomia, Universitá di Bologna, via Gobetti 93/2, I-40122 Bologna, Italy

Accepted 2022 February 8. Received 2022 February 7; in original form 2021 November 12

ABSTRACT

We used the rotation measure (RM) catalogue derived from the LOFAR Two-metre Sky Survey Data Release 2 (LoTSS DR2) at 144 MHz to measure the evolution with redshift of the extragalactic RM (RRM: Residual RM) and the polarization fraction (p) of sources in low-density environments. We also measured the same at 1.4 GHz by cross-matching with the NRAO VLA Sky Survey RM catalogue. We find that RRM versus redshift is flat at 144 MHz, but, once redshift-corrected, it shows evolution at high significance. Also, p evolves with redshift with a decrement by a factor of ∼8 at $z \sim 2$. Comparing the 144-MHz and 1.4-GHz data, we find that the observed RRM and p are most likely to have an origin local to the source at 1.4 GHz, while a cosmic web filament origin is favoured at 144 MHz. If we attribute the entire signal to filaments, we infer a mean rest-frame RRM per filament of $\mathrm{RRM}_{0,\mathrm{f}} = 0.71 \pm 0.07$ rad m^{-2} and a magnetic field per filament of $B_\mathrm{f} = 32 \pm 3$ nG. This is in agreement with estimates obtained with a complementary method based on synchrotron emission stacking, and with cosmological simulations if primordial magnetic fields are amplified by astrophysical source field seeding. The measurement of an $\mathrm{RRM}_{0,\mathrm{f}}$ supports the presence of diffuse baryonic gas in filaments. We also estimated a conservative upper limit of the filament magnetic turbulence of $\sigma_{\mathrm{RRM}_{0,\mathrm{f}}} = 0.039 \pm 0.001$ rad m^{-2}, concluding that the ordered magnetic field component dominates in filaments.

Key words: magnetic fields – polarization – methods: statistical – intergalactic medium – large-scale structure of the Universe.

1 INTRODUCTION

Measuring the evolution of the cosmic magnetic field with cosmic time helps to understand its genesis from primordial fields and whether field seeding and amplification by astrophysical sources has played a role (e.g. Akahori & Ryu 2011; Vazza et al. 2015; Subramanian 2016; Vazza et al. 2017; O'Sullivan et al. 2020; Arámburo-García et al. 2021). Cosmic web filaments are ideal for this purpose, since matter and fields are less processed and closer to the initial conditions. Furthermore, simulations predict that the intensity of filament magnetic fields can help discriminate between the possible scenarios that have magnetized these cosmic structures (e.g. Vazza et al. 2015). The time evolution can also inform us about the evolution of extragalactic sources themselves, such as a change in the physical conditions of the source and its environment (e.g. Kronberg et al. 2008; Berger et al. 2021).

Effective ways to study the magnetic field evolution with time are the behaviour with redshift z of the rotation measure (RM) and the polarization fraction of extragalactic sources. The polarization angle ϕ of linearly polarized radiation travelling through a magnetized, ionized gas is rotated by

$$\Delta\phi = \mathrm{RM}\,\lambda^2 \quad (1)$$

at wavelength λ. RM is

$$\mathrm{RM} = 0.812 \int_z^0 \frac{n_\mathrm{e}(z')B_\parallel(z')}{(1+z')^2}\frac{\mathrm{d}l}{\mathrm{d}z'}\,\mathrm{d}z', \quad (2)$$

where z is the source redshift, the integration is performed from the source to the observer along the path-length l (pc), n_e is the electron density (cm^{-3}), and $B_\parallel$ is the magnetic field along the line of sight (μG). Hence, RM bears information on the magnetized medium the radiation travels through and can be used to trace the evolution of the magnetic field (e.g. Kronberg et al. 2008). The polarization fraction evolution can be related to a change of depolarization (Sokoloff et al. 1998) and, in turn, a change of magneto-ionic physical conditions at the source (e.g. Berger et al. 2021) or in the intergalactic medium (IGM).

The behaviour of the extragalactic source RM with redshift was investigated in the past decades, finding no evolution (Fujimoto,

★ E-mail: carretti@ira.inaf.it

Kawabata & Sofue 1971; Reinhardt 1972; Kronberg, Reinhardt & Simard-Normandin 1977; Sofue, Fujimoto & Kawabata 1979; Kronberg & Perry 1982; Thomson & Nelson 1982; Welter, Perry & Kronberg 1984; Oren & Wolfe 1995; You, Han & Chen 2003; Bernet et al. 2008; Vernstrom et al. 2018; Riseley et al. 2020). However, using samples of a few hundred sources, Kronberg et al. (2008) and Lamee et al. (2016) found a hint of evolution at low significance, at GHz frequencies, which was attributed to RM originating local to the source (Kronberg et al. 2008). This evolution was not confirmed using a much larger sample of 4003 sources (Hammond, Robishaw & Gaensler 2012), making the results inconclusive so far. The evolution of RM with redshift has also been used to investigate the magnetic field of the intracluster medium in galaxy clusters using the differential RM of physical source pairs (Xu & Han 2022).

No clear evolution of fractional polarization was found by Hammond et al. (2012) and Lamee et al. (2016), while Berger et al. (2021) recently found an anticorrelation in a low-brightness sample of 56 sources at 1.4 GHz that was attributed to evolution of the environment local to the source.

The detection of magnetic fields in filaments has been the subject of intense research in recent years (Heald et al. 2020). Several upper limits were set employing a number of different approaches (Brown et al. 2017; Vernstrom et al. 2017; Vacca et al. 2018; O'Sullivan et al. 2019; Vernstrom et al. 2019; O'Sullivan et al. 2020; Locatelli et al. 2021) and a first detection was obtained stacking the synchrotron emission from bridges connecting galaxy clusters (Vernstrom et al. 2021). A direct detection of a filament between a close pair of interacting galaxy clusters was also obtained establishing the presence of magnetic fields in the IGM (Govoni et al. 2019). Cosmological simulations have been run to study the conditions required to generate magnetic fields in filaments that range from a few nG to a few tens of nG depending on whether only primordial fields or additional astrophysical source seeding are involved (Akahori & Ryu 2010, 2011; Gheller et al. 2015; Vazza et al. 2015, 2017; O'Sullivan et al. 2020; Arámburo-García et al. 2021).

In this work, conducted within the LOFAR Magnetism Key Science Project[1] (MKSP), we compute and analyse the behaviour with redshift of the extragalactic source RM and fractional polarization of a low-frequency (144 MHz) RM catalogue (O'Sullivan et al. in preparation). This catalogue was derived from Stokes Q and U data cubes of the LOFAR Two-metre Sky Survey Data Release 2 ((LoTSS DR2; Shimwell et al. 2022; Shimwell et al. 2017, 2019) in a collaborative effort between the LOFAR Surveys Key Science Project[2] and the MKSP. At this low frequency the polarized radiation can survive depolarization only if it is emitted and propagates through low-density environments (O'Sullivan et al. 2019; O'Sullivan et al. 2020; Stuardi et al. 2020), and our analysis allows us to investigate the evolution of magnetism in such environments. We find that an origin of RRM and p in cosmic web filaments is favoured and that enables us to derive properties of the magnetic field in cosmic filaments such as intensity and turbulence.

This paper is organized as follows. Section 2 describes the RM catalogues used in the analysis. Section 3 computes the behaviours with redshift and other related quantities at 144 MHz and 1.4 GHz. Section 4 discusses the results and possible scenarios for the origin of the RM and fractional polarization, and in Section 5, we draw our conclusions.

[1] https://lofar-mksp.org/.
[2] https://lofar-surveys.org/.

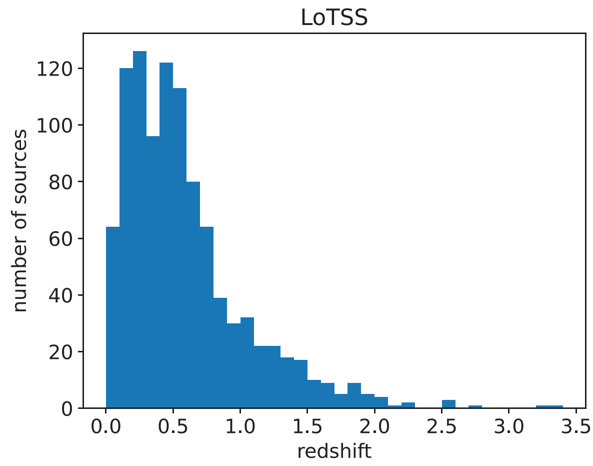

Figure 1. Distribution with redshift of the sources used from the LOFAR LoTSS DR2 RM catalogue.

Throughout this paper, we assume a ΛCDM cosmological model with $H_0 = 67.4\,\mathrm{km\ s^{-1}\ Mpc^{-1}}$, $\Omega_\mathrm{M} = 0.315$, and $\Omega_\Lambda = 0.685$ (Planck Collaboration VI 2020). We also use the term $h = H_0/100\,\mathrm{km\ s^{-1}\ Mpc^{-1}}$.

2 RM CATALOGUES

2.1 LoTSS DR2

Our analysis is based on the RM catalogue derived from Stokes Q and U data cubes of the LoTSS DR2 survey (O'Sullivan et al. in preparation). Here we report the main catalogue features relevant to this work. It consists of 2461 RMs detected at a central frequency of 144 MHz, bandwidth of 48 MHz, channel bandwidth of 97.6-kHz, angular resolution of 20 arcsec, over 5720 deg^2, obtained using the method of RM-synthesis (Brentjens & de Bruyn 2005). The RM error budget is dominated by random ionospheric RM correction residuals, which are $\sim$0.05 rad m^{-2} (O'Sullivan et al. in preparation). A systematic term as large as 0.1–0.3 rad m^{-2} is also present, again related to ionospheric RM correction residuals (Sotomayor-Beltran et al. 2013; Porayko et al. 2019). A total number of 1949 sources had a positive cross-match with redshift catalogues, 1046 of which are spectroscopic redshifts.

Photometric redshifts of the identified sources have a median error of $\sigma_{z,\mathrm{phot}} \sim 0.1$, comparable to the redshift bin width used here, and we excluded them keeping sources with spectroscopic redshift only. A Galactic cut excluding sources at $|b| < 25^\circ$ was applied to exclude the region with highest Galactic RM values, giving 1016 sources.

The source distribution with redshift is shown in Fig. 1. The median redshift is $\sim$0.5. Only a handful of sources have redshift $z > 2$ and we limited our analysis to $z < 2$, for our final sample of 1003 objects.

2.2 NVSS

We also compared the results from the LoTSS RM catalogue with those at higher frequency (1.4 GHz) from the NRAO VLA Sky Survey (NVSS) RM catalogue. The NVSS RM catalogue (Taylor, Stil & Sunstrum 2009) measured the RM of 37 543 sources with two narrow bands, 42-MHz wide each, centred at 1365 and 1435 MHz, and at an angular resolution of 45 arcsec. It covers all Declinations

$\geq -40°$. Hammond et al. (2012) cross-matched it with a number of redshift catalogues obtaining 4003 matches. All redshifts are spectroscopic. To match the selection criteria applied to the LoTSS RM catalogue, we also restricted our NVSS RM sample to sources at Galactic latitudes $|b| > 25°$, resulting in a sample of 3406 sources that reduce to 3055 at the redshift limit of $z < 2$.

Vernstrom et al. (2019) found that RM errors of Taylor et al. (2009) are overestimated for at least part of the sample and we recompute them following their equation (19):

$$\sigma_{\mathrm{RM_{NVSS}}} = 150\,\frac{\sqrt{2}\,\sigma_{\mathrm{P}}}{P}\ \mathrm{rad\,m^{-2}}, \tag{3}$$

with P the polarized intensity of the source, σ_{P} its error, and 150 a coefficient related to the wavelengths of the two NVSS frequency bands.

3 REDSHIFT EVOLUTION ANALYSIS

3.1 LoTSS

The measured RM is the combination of Galactic (GRM), extragalactic, and noise components, where the extragalactic term is either local to the source or from the foreground IGM between the source and the Milky Way, including filaments of the cosmic web:

$$\mathrm{RM} = \mathrm{GRM} + \mathrm{RM_{local}} + \mathrm{RM_{IGM}} + \mathrm{RM_{noise}}. \tag{4}$$

A key point is that the first term has to be subtracted off to be left with the extragalactic component only (and noise), which we call the Residual RM (RRM) :

$$\mathrm{RRM} = \mathrm{RM} - \mathrm{GRM}. \tag{5}$$

We estimate the GRM from Hutschenreuter et al. (2022), who inferred a map of the Galactic RM from a suite of extragalactic source RM catalogues, including those from LoTSS and NVSS. This is a sophisticated evolution of former estimates of GRM maps (e.g. Oppermann et al. 2015) with improved errors, resolution, and sampling of the parent catalogue collection of extragalactic source RMs.

Since the extragalactic RRMs are generally distributed around zero, an estimate of the typical RRM intensity of a sample is the rms deviation $<\mathrm{RRM}^2>^{1/2}$. For the LoTSS sample, if we subtract the GRM contribution as estimated straight from the Hutschenreuter et al. (2022) map at the exact source position, we get an rms deviation of RRM of $<\mathrm{RRM}^2>^{1/2} = 0.52\,\mathrm{rad\ m^{-2}}$ (excluding 2σ outliers), which further drops to $0.15\,\mathrm{rad\ m^{-2}}$ if estimated with the median absolute deviation (MAD) statistics that is more robust against outliers. This is in contrast with the mean GRM error over all sources of $0.79\,\mathrm{rad\ m^{-2}}$. The measured RRM rms is $\langle \mathrm{RRM}^2\rangle^{1/2} = \sqrt{\langle \mathrm{RRM}^2_{\mathrm{source}}\rangle + \langle \mathrm{RRM}^2_{\mathrm{noise}}\rangle}$. The noise term has to be quadratically subtracted off to be left with the source term and a noise larger than the measured term is unexpected. This is possibly because our sample is part of the catalogue suite used to infer the GRM map and the GRM at the exact source position might be slightly biased towards the source RM, which gives an oversubtraction (the possible presence of extragalactic residuals in the GRM map is also mentioned by Hutschenreuter et al. 2022). Actually, an inspection of the GRM map shows that it can have a slight bump at our source positions compared to the immediate surrounding fields.

To test this further, for each source ,we computed the difference of RM and GRM with a reference term. As a reference we used $\mathrm{GRM_1}$, the median of the GRM map over a 1° diameter disc centred at the source position that is approximately the average spacing between sources in the catalogue suite used by Hutschenreuter et al. (2022). The differences are

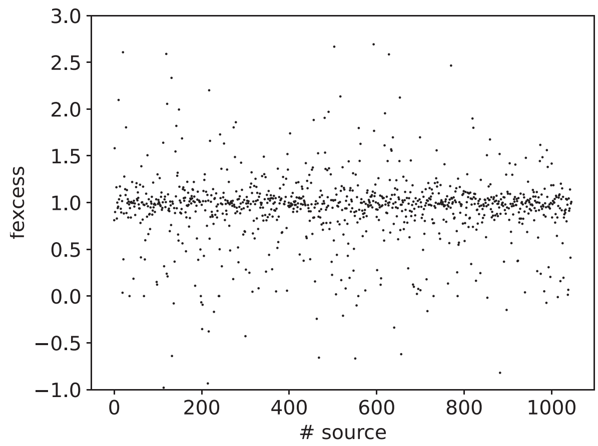

Figure 2. Fractional excess f_{excess} (equation 8) of each individual source of the selected LoTSS DR2 RM catalogue sample.

$$\mathrm{RM_{excess}} = \mathrm{RM} - \mathrm{GRM_1}, \tag{6}$$

$$\mathrm{GRM_{excess}} = \mathrm{GRM} - \mathrm{GRM_1}. \tag{7}$$

Their ratio, the fractional excess,

$$f_{\mathrm{excess}} = \frac{\mathrm{RM_{excess}}}{\mathrm{GRM_{excess}}}, \tag{8}$$

is shown in Fig. 2. Its median is $\bar{f}_{\mathrm{excess}} = 0.986 \pm 0.005$ and has a narrow deviation of $\sigma_{f_{\mathrm{excess}}} = 0.15$ (here we used the median and its deviation as estimated with the MAD statistics because they are more robust against the obvious outliers). This means it tends to be RM = GRM for each individual source and suggests that GRM actually is slightly biased towards the source RM at its exact position.

Instead, to estimate the GRM we have then taken $\mathrm{GRM_1}$ as defined above, because the median over a region around the source tends to mitigate the contribution of the bump at the source position (applying a smoothing is also recommended by Hutschenreuter et al. 2022). The distribution of the RRMs obtained with the GRMs so estimated is shown in Fig. 3. The RRM rms corrected for the noise is

$$\left\langle \mathrm{RRM_{LoTSS}}^2 \right\rangle^{1/2} = 1.90 \pm 0.05\ \mathrm{rad\,m^{-2}}, \tag{9}$$

where the noise terms are the RM measurement noise and the $\mathrm{GRM_1}$ error quadratically subtracted off. Because of the presence of outliers, here and throughout this paper, RRMs that are off by more than 2σ were excluded. This result is broadly consistent with O'Sullivan et al. (2020), who estimated the differential RM rms of random pairs at the same frequency, which is $\sqrt{2}$ times the RRM rms of a single source. Dividing their result by $\sqrt{2}$ (we used their result on 42 random pairs within 10-arcmin separation), we estimate an RRM rms of single sources of

$$\left\langle \mathrm{RRM}^2_{\mathrm{rp}} \right\rangle^{1/2} = 1.3 \pm 0.2\ \mathrm{rad\,m^{-2}}, \tag{10}$$

which supports that the procedure applied here is correct.

Fig. 4, top panel, and Table 1 report the RRM mean of the LoTSS sample in equal-width redshift bins. It is zero within 2σ in all bins.

Fig. 4, bottom panel, and Table 1 report the RRM rms deviation $\langle \mathrm{RRM}^2\rangle^{1/2}$ in the same redshift bins (red solid line). It is flat with

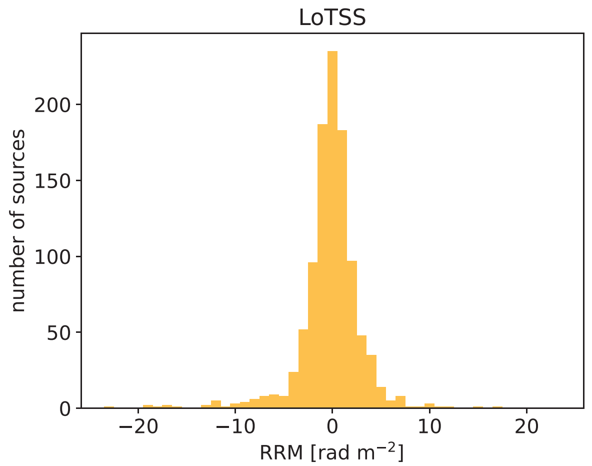

Figure 3. Distribution of RRMs of the sample from the LoTSS RM catalogue.

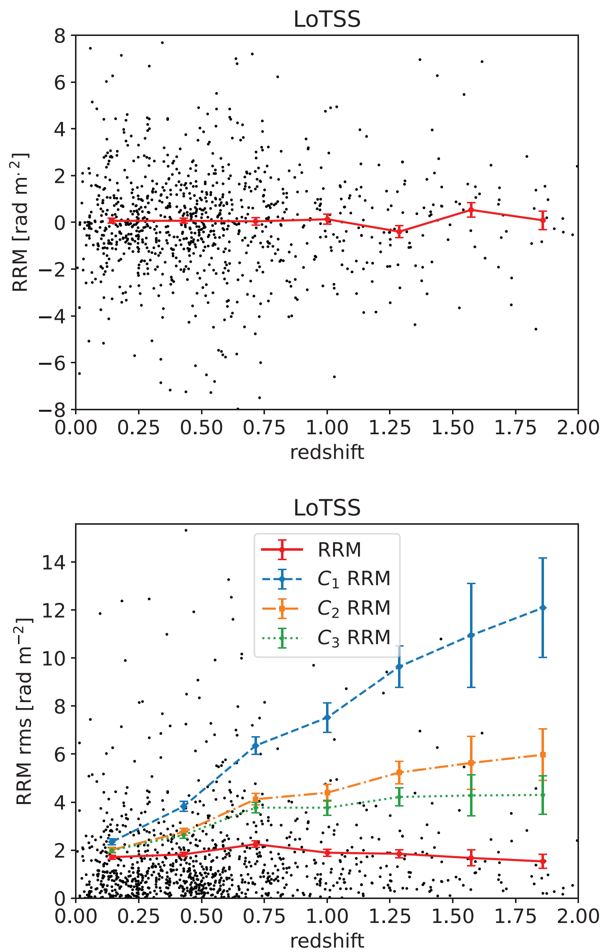

Figure 4. Top panel: mean of the RRM sample selected from the LoTSS RM catalogue in equal-width redshift bins (red solid line). Individual RRMs are also shown (dots). Bottom panel: as for the top panel but for the RRM rms deviation (red solid line). The rest-frame RRM_0 corrected for the redshift effects C_1 (dashed line), C_2 (dot–dashed line), and C_3 (dotted line) are also plotted. Individual |RRM|s are shown as dots.

redshift, its linear fit gives a slope of $\beta = -0.15 \pm 0.15$, consistent with no evolution with redshift out to $z = 2$. Here and throughout this paper, the error terms (i.e. the RM measurement noise and the GRM_1 error) are quadratically subtracted off from the RRM rms estimates.

The RRMs must be corrected for redshift effects to get the rest-frame RRM_0 (see equation 2). Specifically ,

$$\mathrm{RRM}_0 = \mathrm{RRM}(1 + z_i)^2, \tag{11}$$

where $z_i <= z$ is the redshift at which the Faraday Rotation occurs along the line of sight and z the source redshift. If the RRM is generated at more locations along the line of sight, then

$$\mathrm{RRM}_0 = \sum_i \Delta\mathrm{RRM}_i\, (1 + z_i)^2, \tag{12}$$

where $\Delta\mathrm{RRM}_i$ is the RRM contribution at redshift z_i. What those redshifts are depends on how the medium is organized along the line of sight. RRM_0 can be written as

$$\mathrm{RRM}_0 = C_x\ \mathrm{RRM}, \tag{13}$$

where C_x is a correction factor depending on a model x of the medium distribution.

Three example cases bracket most of the possible models.

(i) In the simplest case the RRM occurs close to the source, either internal to the source or in the surrounding medium. This gives

$$C_1 = (1 + z)^2, \tag{14}$$

where z is the source redshift.

(ii) At the other end, we have the case in which the non-redshift-corrected RRM is generated evenly along the line of sight, which is the IGM in the foreground. This gives

$$C_2 = \frac{1}{z}\int_0^z (1 + z')^2\, \mathrm{d}z' \tag{15}$$

$$= \frac{(1 + z)^3 - 1}{3z}. \tag{16}$$

(iii) A third case is similar to (ii), except it is the rest-frame RRM_0 that is evenly distributed. More specifically, the two models differ on how RRM is distributed along the sight line. This model also describes the IGM and includes the scenario in which the RRM is generated by many cosmic web filaments along the line of sight. It gives

$$C_3 = 1 + z. \tag{17}$$

Fig. 4, bottom panel, and Table 1 report the RRM rms in redshift bins corrected for C_1, C_2, and C_3. Data were first corrected and then binned. To check whether the increase with redshift is significant we fit them with a linear model, with the results shown in Table 2. The slope β is non-flat at high significance for all three cases (β/σ_β = 22.0, 10.7, and 4.9, respectively, where σ_β is the error of β) with Student's t-test probabilities of $p_t = 1.8 \times 10^{-6}$, 6.2×10^{-5}, and 2.2×10^{-3}. Accounting for the redshift correction, there is evolution of RRM_0 with redshift at high significance in the range $0 < z < 2$ for all models we have considered. Spearman tests were also conducted with consistent results (see Table 2).

The analysis was repeated excluding the sources close to the Galactic plane for different Galactic latitude (b) cuts. Fig. 5 shows the case of RRM_0 with correction C_1. The behaviours are similar and the increase with redshift z is present at all cuts. This excludes significant systematics from residual Galactic RM contamination, especially from the sources at lower $|b|$.

We computed the RRM mean and rms deviation also in redshift bins with equal number of sources, with consistent results (see Appendix A).

An analysis of the fractional polarization evolution can help us with the interpretation because a change with redshift would mean a

Table 1. RRM mean and rms of the LoTSS sample in the equal-width redshift bins z (bin centre). The rms of the rest-frame $\mathrm{RRM}_0 = C_x$ for the three redshift correction models C_x discussed in the text are also reported.

z	$\langle \mathrm{RRM} \rangle$ (rad m^{-2})	$\langle \mathrm{RRM}^2 \rangle^{1/2}$ (rad m^{-2})	$\langle (C_1\ \mathrm{RRM})^2 \rangle^{1/2}$ (rad m^{-2})	$\langle (C_2\ \mathrm{RRM})^2 \rangle^{1/2}$ (rad m^{-2})	$\langle (C_3\ \mathrm{RRM})^2 \rangle^{1/2}$ (rad m^{-2})
0.143	0.06 ± 0.10	1.71 ± 0.09	2.34 ± 0.12	2.01 ± 0.10	1.99 ± 0.10
0.429	0.07 ± 0.11	1.82 ± 0.09	3.82 ± 0.21	2.75 ± 0.14	2.63 ± 0.13
0.715	0.04 ± 0.17	2.25 ± 0.14	6.35 ± 0.37	4.12 ± 0.23	3.77 ± 0.22
1.001	0.13 ± 0.21	1.89 ± 0.15	7.52 ± 0.62	4.39 ± 0.37	3.77 ± 0.31
1.287	− 0.40 ± 0.25	1.85 ± 0.16	9.64 ± 0.90	5.23 ± 0.46	4.21 ± 0.39
1.573	0.53 ± 0.32	1.67 ± 0.34	10.95 ± 2.15	5.63 ± 1.09	4.28 ± 0.86
1.859	0.09 ± 0.39	1.53 ± 0.28	12.09 ± 2.17	5.97 ± 1.06	4.30 ± 0.76

Table 2. Linear best-fitting parameters of the rest-frame RRM_0 rms of the LoTSS sample for the three models C_x, $x = 1, 2, 3$. The fit function is $\mathrm{RRM}_0 = \alpha + \beta z$, with α the intercept and β the slope. The other parameters of the Table are the ratio t between β and its error σ_β, the Student's t-test probability that $t = 0$ – i.e. β is flat (p_t), the Spearman's rank correlation coefficient ρ between RRM_0 rms and z, and its probability of uncorrelation (p_ρ).

Model	α (rad m^{-2})	β (rad m^{-2})	$t = \beta/\sigma_\beta$	p_t	ρ	p_ρ
C_1	1.68 ± 0.31	5.84 ± 0.27	22.0	1.8 10^{-6}	1.00	0.0
C_2	1.96 ± 0.25	2.34 ± 0.22	10.7	6.2 10^{-5}	1.00	0.0
C_3	2.23 ± 0.31	1.33 ± 0.27	4.9	2.2 10^{-3}	0.96	4.5 10^{-4}

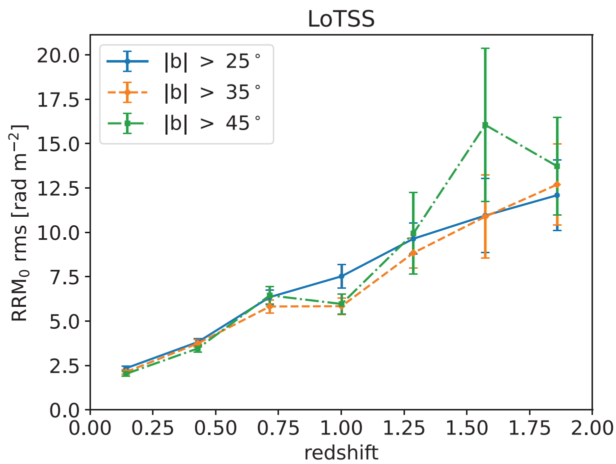

Figure 5. RRM_0 rms corrected for C_1 excluding sources at three different Galactic latitude (b) cuts.

change of the physical conditions at the sources or of the IGM over cosmic time. Fig. 6, top panel, shows $\langle \mathrm{RRM}^2 \rangle^{1/2}$ as a function of the fractional polarization p, with no obvious correlation. The mean of the fractional polarization as a function of redshift is also shown in Fig. 6, bottom panel. There is clear anticorrelation: p is highest at low z (some 5 per cent at $z = 0.1$) and steadily drops towards high redshift (0.65 per cent at $z = 1.9$). The behaviour is close to linear in $\log(p)$-z space, the slope of the linear regression is $\beta = -0.396 \pm 0.044$ with ratio $\beta/\sigma_\beta = 9.0$ and t-test $p_t = 8.9 \times 10^{-6}$. The Spearman's rank is $\rho = -0.96$ and $p_\rho = 7.3 \times 10^{-6}$. The decrease is thus detected at a high confidence level.

The mean source angular size in redshift bins is reported in Fig. 7. Only 269 sources have size information available. A decrement with z is obvious from ≈500 arcsec at $z = 0.1$ to ≈70 arcsec at $z = 1.9$, making a correlation with depolarization possible. We computed also the physical sizes. The sources are very extended on average with mean sizes that run from ∼1.3 Mpc at low redshift to ∼0.7 Mpc at high redshift. It is clear that the objects for which the size information is available (269 out of 1003, 27 per cent) are only extended sources and with the compact sources absent from this sub-sample.

We separated the sources into blazars and radio galaxies (i.e. all other radio sources such as radio galaxies, Seyferts, QSOs, AGN) to broadly divide them in compact and extended sources. We used the classification from the BZCAT blazar catalogue (Massaro et al. 2015),[3] SIMBAD data base,[4] and Sloan Digital Sky Survey (SDSS) DR16 catalogue (Ahumada et al. 2020)[5] – with this priority, respectively – included in the LoTSS RM catalogue. All sources of our sample have a classification, of which 17 per cent are blazars. Radio galaxies dominate except at $z \gtrsim 1.5$ where the number of blazars becomes comparable.

3.2 NVSS

The RRMs of the NVSS RM–redshift catalogue (Hammond et al. 2012) were computed estimating the GRM as in Section 3.1.

The RRM dispersion of the entire sample, corrected for the RM measurement error and the GRM_1 error, is

$$\langle \mathrm{RRM}^2_{\mathrm{NVSS_{all}}} \rangle^{1/2} = 13.28 \pm 0.27\ \mathrm{rad\,m^{-2}}. \tag{18}$$

This is much larger than for the LoTSS sample, possibly because of the smaller depolarization at higher frequency and hence the source population comes from a more diverse environment. At higher frequencies, the polarized emission can survive after passing through higher density environments and hence develop higher RMs (O'Sullivan et al. 2020; Stuardi et al. 2020)

[3] https://www.ssdc.asi.it/bzcat/.
[4] http://simbad.u-strasbg.fr/simbad/.
[5] https://www.sdss.org/dr16/.

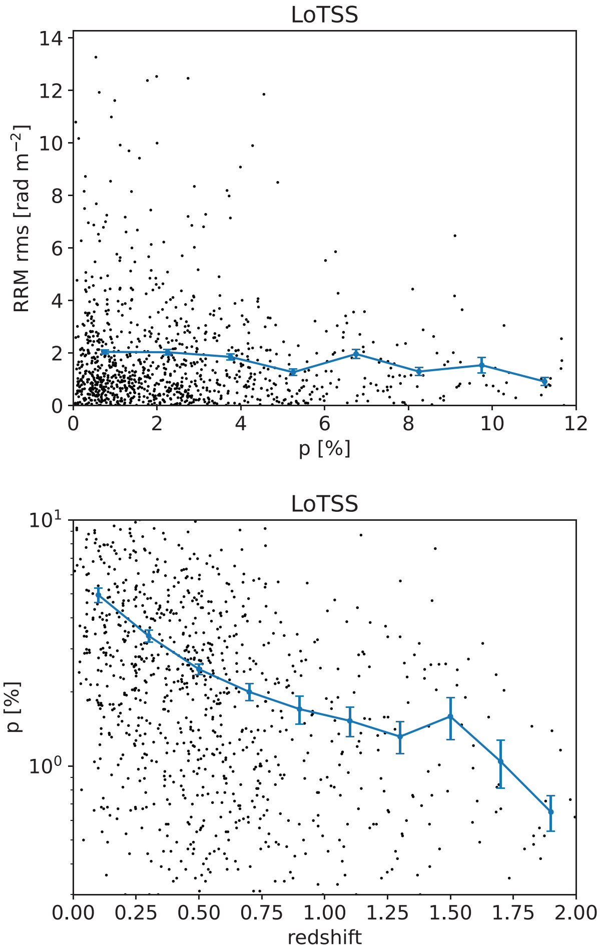

Figure 6. Top panel: RRM rms deviation as a function of fractional polarization p of the LoTSS sample (solid line). Individual |RRM|s are also reported (dots). Bottom panel: mean of the fractional polarization p as a function of z of the LoTSS sample (solid line). Individual fractional polarizations are also reported (dots).

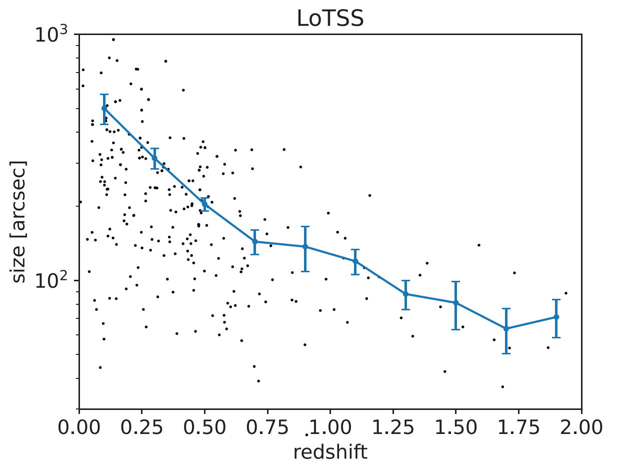

Figure 7. Mean source angular size as a function of z of the LoTSS sample (solid line). Individual sizes are also reported (dots).

Fig. 8, top panel, shows the RRM rms deviation in redshift bins. The behaviour is flat before correcting for redshift effects, while after correction with models C_1, C_2, and C_3, an evolution with z is obvious, albeit with smaller confidence compared to the LoTSS sample. Both linear fit and Spearman rank results are reported in Table 3.

The middle panel of Fig. 8 shows RRM rms versus fractional polarization p. There is a clear anticorrelation, a decrease of RRM, initially steeper and then shallower. This behaviour is similar to the result of Hammond et al. (2012), who found an anticorrelation up to the same p-value and then a flattening close to their noise floor that they did not subtract in their plots. They associated that anticorrelation with depolarization: higher RRMs means the polarized radiation goes through higher density and higher magnetic field environments, which gives higher depolarization.

The fractional polarization p versus redshift (Fig. 8, bottom panel) decreases up to $z \sim 0.7$, then it is mostly flat (as found by Hammond et al. 2012). This differs from the LoTSS sample where p decreases with z for the entire range.

3.3 LoTSS – NVSS overlap sample

To better compare the NVSS and LoTSS samples, we have selected the LoTSS RM catalogue sources with an NVSS RM entry and a spectroscopic redshift, and then analysed the NVSS RMs at 1.4 GHz. This NVSS sub-sample is thus restricted to the LoTSS sample and we call it the NVSS/LoTSS sample. It consists of 437 sources, 427 of which have $z < 2$.

The RRM rms of this sample is

$$\left\langle \mathrm{RRM}^2_{\mathrm{NVSS/LoTSS}} \right\rangle^{1/2} = 5.72 \pm 0.36 \ \mathrm{rad\,m^{-2}}. \tag{19}$$

This is less than half the value derived for the whole NVSS sample, confirming that the LoTSS low-frequency catalogue selects for low-density environments that generate lower RRMs.

Fig. 9 shows the RRM rms as a function of z and p, and p as a function of redshift. It is worthwhile to note some differences of these 1.4-GHz RRMs that are in low-density environments. The RRM rms has a gentle increase with z, which is unseen in both the LoTSS and the whole NVSS sample. The increase is marginally significant with a slope that differs from zero by 3.3 σ and a p-value of $p_t = 1.1 \times 10^{-2}$. The redshift-corrected RRM$_0$ has a high significance detection of an evolution with z for all models we considered (Table 4).

The RRM anticorrelates with p, as in the NVSS case and differing from the LoTSS sample, up to $p \sim 8$ per cent and then it flattens. The fractional polarization decreases with z at high significance, as at 144 MHz, albeit at a lower rate (a factor of ∼3 between the two redshift range ends instead of ∼8), but different from the whole 1.4-GHz sample that shows an initial evolution only. All points except one follow the decreasing trend and that single point is at some 1σ from the general trend. A linear–log space linear fit gives a slope of $\beta = -0.242 \pm 0.029$ with ratio $\beta/\sigma_\beta = 8.3$ and p-value of $p_t = 1.7 \times 10^{-5}$. Spearman's rank is $\rho = -0.96$, $p_\rho = 7.3 \times 10^{-6}$.

We also separated the sources into blazars and radio galaxies, as done for the LoTSS sample. All of the sources in the NVSS/LoTSS sample have classifications, with 25 per cent being blazars. The redshift distributions of the two groups are shown in Fig. 10, where radio galaxies dominate out to $z \approx 0.9$, above which blazars become comparable or dominant.

The large difference between the RRM rms at 144 MHz and 1.4 GHz (1.9 and 5.7 rad m^{-2}) suggests the RRMs at the two

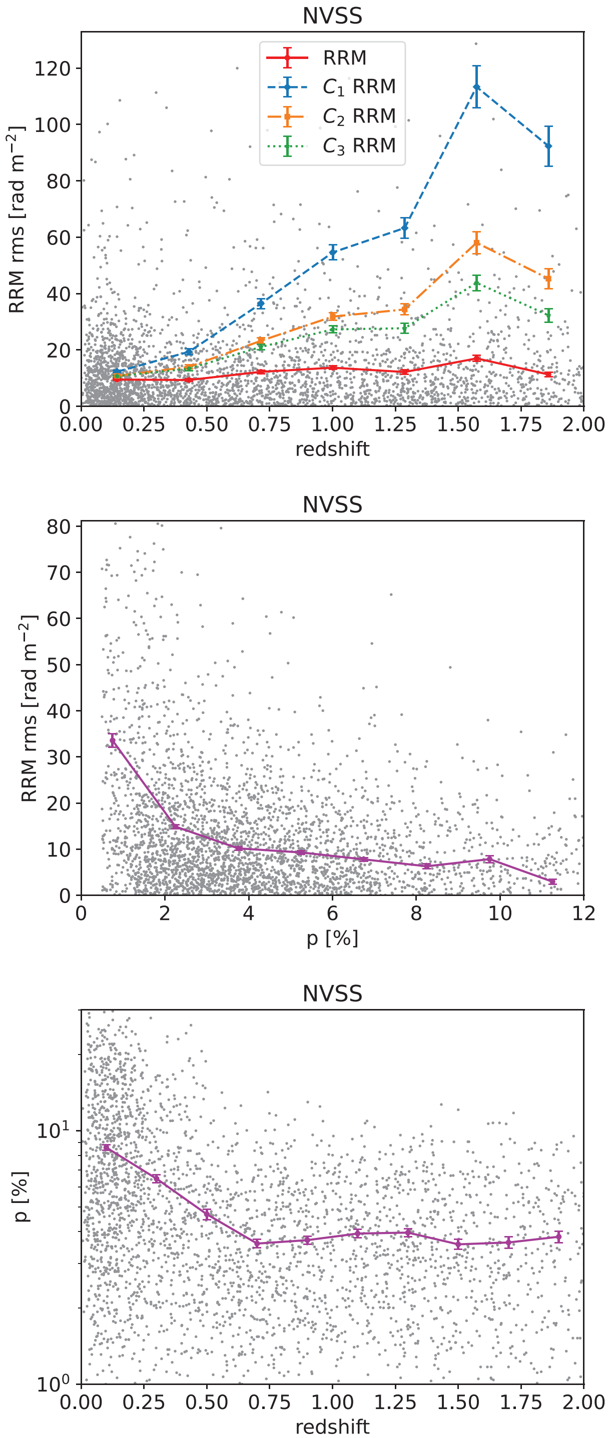

Figure 8. Top panel: NVSS sample RRM rms deviation in redshift bins (red solid line). The rest-frame RRM_0 corrected for the redshift effect C_1 (dashed line), C_2 (dot–dashed line), and C_3 (dotted) are also plotted. The individual |RRM|s are reported as dots. Middle panel: RRM rms deviation as a function of fractional polarization p for the NVSS sample (solid line). Individual |RRM| values are also reported (dots). Bottom panel: mean of fractional polarization p as a function of z for the NVSS sample (solid line). Individual fractional polarization values are also shown (dots).

frequencies are different. In Fig. 11, we plot them against each other. Indeed, the sources appear randomly distributed with no obvious trend, which would indicate the two sets of RRMs are different and thus of different origin. However, the large NVSS error bars cover most of the spread preventing us from drawing firm conclusions.

4 DISCUSSION

4.1 Environment

The low RRM rms of $\sim$1.9 rad m^{-2} that we measure for the LoTSS sample supports that the polarized emission at low frequency comes from and propagates through low-density environments, where it can survive depolarization, as found in earlier work (e.g. O'Sullivan et al. 2020; Stuardi et al. 2020). This also appears to be supported by the higher frequency NVSS sample (1.4 GHz) that, once restricted to the sources in common with the LoTSS catalogue, has an RRM rms approximately two times smaller than the full sample.

To further support these considerations, we measured the projected separation in R_{200}[6] units for our sources from the nearest galaxy cluster, for both LoTSS and NVSS samples, where R_{200} is approximately the outer boundary of galaxy clusters. We use the catalogue of 158,103 clusters by Wen & Han (2015) (see also Wen, Han & Liu 2012) that spans $0.05 < z < 0.75$ and has a mix of spectroscopic and photometric redshifts with errors up to 0.018. Masses of catalogue clusters are as low as 2×10^{12}M$_\odot$ and the catalogue is more than 95 per cent complete for masses larger than 1.0×10^{14}M$_\odot$, which covers well down to poor clusters. Note that the catalogue gives R_{500}[7] for each galaxy cluster and we estimate R_{200} by the relation $R_{500}/R_{200} \approx 0.7$ (Ettori & Balestra 2009). For each source of redshift z_s, we search for the galaxy cluster with minimum projected separation in the redshift range $|z_{gc} - z_s| < 0.036$ (2σ uncertainty), where z_{gc} is the cluster redshift. We restrict our search to sources with redshift in the catalogue range and that are in the catalogue footprint, resulting in 739 (LoTSS) and 1116 (NVSS) sources. The minimum projected separation distributions are shown is Fig. 12. Only a small fraction of sources (6.2 per cent) in the LoTSS sample is within R_{200} from the nearest cluster, which increases to 21.5 per cent for the NVSS sample. The median separation is 7.0 and 5.2R_{200} for LoTSS and NVSS, respectively. The distribution of the LoTSS sample peaks at $\sim 5R_{200}$ and then decreases towards separation 0, while for the NVSS sample it is mostly flat down to the smallest separations, meaning that the peak is closer to separation 0. Overall, the 144-MHz LoTSS sources tend to reside far from galaxy clusters, in low-density environments, while the 1.4-GHz NVSS sources are closer to clusters with a marked peak within cluster boundaries. We do not have available an equivalent catalogue of galaxy groups and we cannot conduct a similar analysis for them.

Considerations based on simple depolarization models bear similar conclusions. These are approximations of real cases, but are useful to give first-order estimates. As mentioned previously, the extragalactic RM can be generated locally to the source or by the IGM through which the radiation propagates. In the former case, most of the RM and p are generated in the environment surrounding the source (Laing et al. 2008). Both this and the radiation propagating through the IGM can be modelled by a turbulent slab (external Faraday

[6] R_{200} is the distance from the cluster centre where the density drops to 200 times the critical density of the Universe.
[7] R_{500} is the distance from the galaxy cluster centre where the density is 500 times the critical density of the Universe.

Table 3. Linear best-fitting parameters of the rest-frame RRM_0 rms of the NVSS sample for the three models C_x, $x = 1, 2, 3$. The fit function is $RRM_0 = \alpha + \beta z$, with α the intercept and β the slope. The other parameters of the Table are the ratio between β and its error σ_β (t), the Student's t-test probability that $t = 0$, i.e. β is flat (p_t), the Spearman's rank correlation coefficient ρ between RRM_0 and z, and its probability of no correlation (p_ρ).

Model	α (rad m^{-2})	β (rad m^{-2})	$t = \beta/\sigma_\beta$	p_t	ρ	p_ρ
C_1	-0.91 ± 10.26	56.80 ± 8.90	6.4	$7.0\ 10^{-4}$	0.96	$4.5\ 10^{-4}$
C_2	5.74 ± 5.25	25.32 ± 4.55	5.6	$1.3\ 10^{-3}$	0.96	$4.5\ 10^{-4}$
C_3	8.64 ± 4.17	16.53 ± 3.62	4.6	$3.0\ 10^{-3}$	0.96	$4.5\ 10^{-4}$

dispersion) whose depolarization is described by the equation (Burn 1966; Sokoloff et al. 1998):

$$\frac{p}{p_0} = e^{-2\sigma_{RM}^2 \lambda^4}, \quad (20)$$

where p and p_0 are the emerging polarization fraction and that of the radiation entering the region, respectively. The σ_{RM} parameter is the RM dispersion of the region, and λ is the observing wavelength. Assuming the signal is totally depolarized for[8] $p/p_0 = 1/30$, the signal can survive depolarization at 144 MHz for $\sigma_{RM} \langle 0.3$ rad m^{-2}, which sets a small limit for the RM turbulence it can go through and thus requires low-density environments.

4.2 Fractional polarization behaviour

There is a clear evolution with redshift of p and of the rest-frame RRM_0 for the LoTSS sample, for any redshift correction model we use. This might happen local to the source or in the IGM along the line of sight. A comparison with the results at 1.4 GHz can help with the interpretation.

Fig. 13, left-hand panel, shows the behaviour of p versus z for all of our three samples. LoTSS has the lowest values with a steady decrement with redshift, while NVSS has higher values that, after an initial decrement, becomes flat. NVSS/LoTSS is always higher than NVSS, as expected since the emission is coming from lower density environments, and it shows a steady decrease with redshift, similar to LoTSS, albeit at a significantly lower rate.

There are two possible explanations for the depolarization behaviour of the LoTSS sample, an astrophysical origin or beam depolarization because the source size gets smaller at higher redshift (Fig. 7). The latter is a frequency-independent effect. The decrease of $p(z)$ and its flattening at high redshift for the NVSS sample was interpreted by Hammond et al. (2012) as a mixing of two populations with different polarization fractions: radio galaxies at low redshift and compact sources that have a lower polarization fraction at high redshift. The NVSS/LoTSS sample has a continuous decrement with redshift. Radio galaxies are the dominant population up to $z \sim 0.9$ and beam depolarization could explain it, but at $z > 0.9$ blazars are comparable or dominate and a flattening would be expected. Similarly, the LoTSS sample has a transition at $z \sim 1.5$, but no flattening is observed. In this context, we note that the angular diameter distance peaks at $z \sim 1.5$ and is quite flat in the range $z = [1, 2]$, thus beam depolarization alone cannot explain the drop of p in that range. Finally, for the NVSS/LoTSS sample, that traces the similar environments of the full LoTSS sample, p anticorrelates with redshift as for LoTSS, but at a smaller rate, thus at most only a minor component can be due to frequency-independent depolarization. Note that the coarser beam at 1.4 GHz can generate more depolarization and correcting for it would further increase the difference in the p decrement rate between the two frequencies, reinforcing the conclusion that only a minor component of the depolarization at 144 MHz can be attributed to beam depolarization. We conclude that beam depolarization is unlikely to be the cause of most of the behaviour with redshift for p, leaving the astrophysical origin as the most likely explanation. An anticorrelation at 1.4 GHz was also found by Berger et al. (2021) with a much smaller, lower flux sample and they too excluded beam depolarization.

As mentioned, the astrophysical origin of the p–z anticorrelation can be either local to the source or in the IGM between us and the source. At 1.4 GHz, we can exclude the latter as the dominant term. The depolarization of the NVSS/LoTSS sample at $z = 1.9$ is $p/p_0 \sim 30$ per cent, measured as the ratio of the mean of p at the high- and low-redshift end. If this is due to the IGM, from equation (20) the depolarization would drop to 0.003 per cent at 144 MHz and we would not see any polarized signal. Hence, the depolarization observed at 1.4 GHz must be local to the source and the components observed at 144 and 1400 MHz must be of a different nature. The component that we see at 144 MHz has almost no depolarization at 1.4 GHz. At 144 MHz, the depolarization is still compatible with either possible origin, and thus not inconsistent with being generated by the IGM. We expect the IGM to consist of filaments whose number increases with z leading to increasing depolarization with z. Among local origin effects, a couple can be excluded. At both 144 and 1400 MHz, the behaviour of p is unlikely to be due to a change of population with redshift. As mentioned above, a flattening would be expected at high redshift, which is not observed. Also, effects from external Faraday dispersion (equation 20) are unlikely because at high redshifts, the rest-frame frequency is higher by a factor of $(1 + z)^2$ and the depolarization is expected to be smaller, while the opposite is observed.

The behaviour of RRM versus p is different at 144 and 1400 MHz (Fig. 13, right-hand panel, shows all of the three samples). It is anticorrelated with p at 1400 MHz for both the NVSS and NVSS/LoTSS sample. That behaviour was associated by Hammond et al. (2012) with the effect of depolarization: higher RRMs means the polarized radiation goes through higher density and higher magnetic field environments.This usually gives higher turbulence and RRM dispersion, and in turn higher depolarization (e.g. equation 20). This points to the RRM being generated at the source at 1.4 GHz. At 144 MHz, it is flat and the RRM is independent of depolarization. This is a totally different behaviour and again points to the RRM generation mechanism being different to that at higher frequency. Cosmological MHD simulations find that the RRM generated by filaments of the cosmic web along the line of sight is mostly independent of redshift

[8]We assumed this value because a depolarization of 10 per cent looked insufficient and 1 per cent too much at this frequency where the typical fractional polarization is of a few per cent.

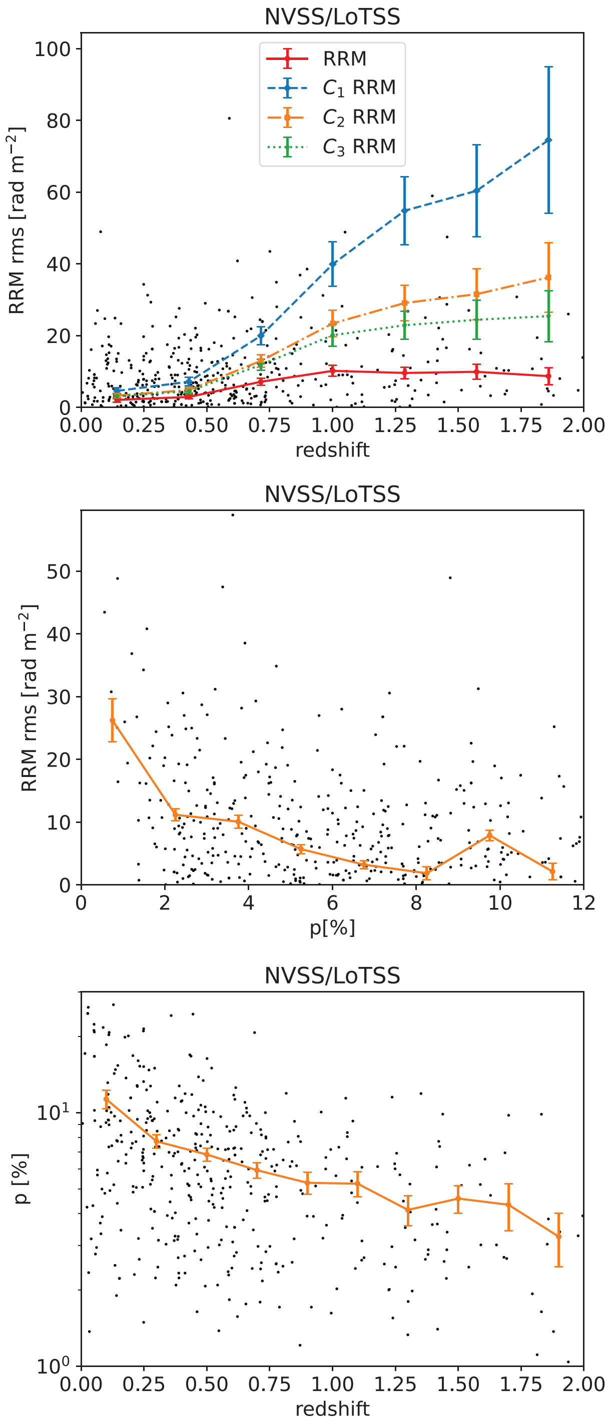

Figure 9. Top panel: NVSS/LoTSS sample RRM rms deviation as a function of redshift (red solid line). The rest-frame RRM_0 corrected for the redshift effect C_1 (dashed line), C_2 (dot–dashed line), and C_3 (dotted line) are also plotted. Individual |RRM| values are reported as dots. Middle panel: RRM rms deviation as a function of fractional polarization p for the NVSS/LoTSS sample (solid line). Individual |RRM| are also reported (dots). Bottom panel: mean of fractional polarization p as a function of z for the NVSS/LoTSS sample (solid line). Individual fractional polarization are also reported (dots).

(Akahori & Ryu 2011), because the increase of rest-frame RRM_0 with redshift (because of the higher number of filaments intercepted) is compensated by the redshift correction. RRM is also expected to be independent of p because RRM is uncorreleted with z while p changes. The flat behaviour of RRM versus p and z is thus consistent with that expected for a IGM/filaments scenario at 144 MHz and against a local origin. Notice that for the 1.4-GHz NVSS/LoTSS sample, the RRM marginally increases with redshift, inconsistent with a generation dominated by the IGM.

In the next sections, we analyse in detail the two possible scenarios at 144 MHz that could explain the behaviour that we observe for p, RRM, and RRM_0.

4.3 IGM filaments

Several arguments, as described above, point to the RRM and p we observe at 144 MHz being consistent with a generation from filaments of the cosmic web, e.g. the flat behaviour of RRM with p and z. Assuming that, we can derive some properties of the magnetic field of filaments.

The depolarization is expected to follow a similar behaviour as described by equation (20) for the propagation of the polarized emission through cosmic web filaments, which can be written as

$$\frac{p}{p_0}(z) = \mathrm{e}^{-2\,\sigma^2_{\mathrm{RRM}_{0,\mathrm{f}}}\,N_\mathrm{f}(z)\,\lambda^4}, \tag{21}$$

where $\sigma_{\mathrm{RRM}_{0,\mathrm{f}}}$ is the average σ_{RM} of a single filament and N_f the number of filaments the radiation goes through. The term p_0 is taken from the linear fit of p at $z = 0$ (Section 3.1). We estimate the number of filaments intercepted by each source of the LoTSS sample using the filaments catalogues of Chen et al. (2015) and Carrón Duque et al. (2021) that extend out to $z = 0.7$ and 2.2, respectively. The catalogues cover the area of the Sloan Digital Sky Survey (SDSS) and 745 sources of our LoTSS sample fall in it. We assume a typical filament transverse width of 3 Mpc (Cautun et al. 2014). The number of filaments intercepted by the individual sources versus their redshift and their quadratic fit

$$N_\mathrm{f}(z) = -1.08\,z^2 + 17.89\,z - 0.37 \tag{22}$$

are shown in Fig. 14.

The best fit of equation (21) to the depolarization as a function of z of the LoTSS sample is shown in Fig. 15, left-hand panel. The curve fits the data well, further supporting the cosmic web filament origin of the depolarization. The best estimate of $\sigma_{\mathrm{RRM}_{0,\mathrm{f}}}$ is

$$\sigma_{\mathrm{RRM}_{0,\mathrm{f}}} = 0.0389 \pm 0.0010\ \mathrm{rad\,m^{-2}}, \tag{23}$$

which gives an estimate of the average RM turbulence of filaments (the first to our knowledge). We regard this as an upper limit because part of the depolarization might be of a different origin. It is a conservative upper limit, for a cosmic filament origin is favoured and $\sigma_{\mathrm{RRM}_{0,\mathrm{f}}}$ is at least 50 per cent of our estimate.

If the RRM is generated by the filaments, then its rms deviation is expected to be mostly flat with z (Akahori & Ryu 2011), as we observe at 144 MHz, and $\langle \mathrm{RRM}_0^2 \rangle^{1/2}$ is expected to increase with redshift as $N_\mathrm{f}^{1/2}(z)$ (Akahori & Ryu 2010) because the path-length through the filaments is a random walk and the RRM of each filament can be either negative or positive. The best redshift correction for filaments is C_3, as discussed in Section 3.1. We fit the RRM_0 rms values that we measure with equal-width redshift bins for the LoTSS sample with the function :

$$\mathrm{RRM}_0(z) = \mathrm{RRM}_{0,\mathrm{f}}\ N_\mathrm{f}^{1/2}(z) + A_{\mathrm{RRM}}, \tag{24}$$

Table 4. Linear best-fitting parameters of the rest-frame RRM_0 rms of the NVSS/LoTSS sample for the three models C_x, $x = 1, 2, 3$. The fit function is $RRM_0 = \alpha + \beta z$, with α the intercept and β the slope. The other parameters of the table are the ratio between β and its error σ_β (t), the Student's t-test probability that $t = 0$, i.e. β is flat (p_t), the Spearman's rank correlation coefficient ρ between RRM_0 and z, and its probability of no correlation (p_ρ).

Model	α (rad m^{-2})	β (rad m^{-2})	$t = \beta/\sigma_\beta$	p_t	ρ	p_ρ
C_1	-6.5 ± 3.5	43.8 ± 3.1	14.3	$1.5\ 10^{-5}$	1.00	0.00
C_2	-0.8 ± 2.1	21.0 ± 1.8	11.7	$3.9\ 10^{-5}$	1.00	0.00
C_3	1.3 ± 2.3	14.7 ± 2.0	7.5	$3.3\ 10^{-4}$	1.00	0.00

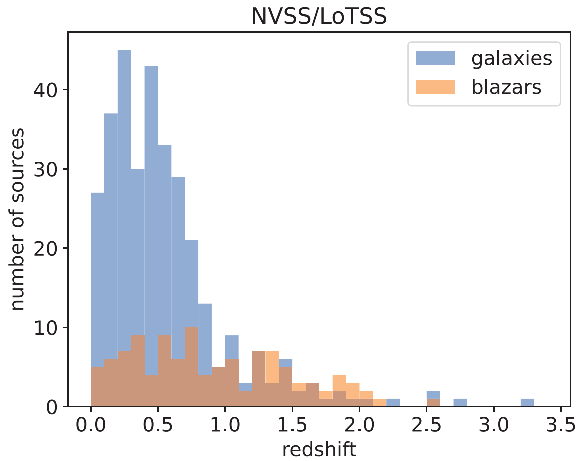

Figure 10. Redshift distribution of radio galaxies and blazars of the NVSS/LoTSS sample.

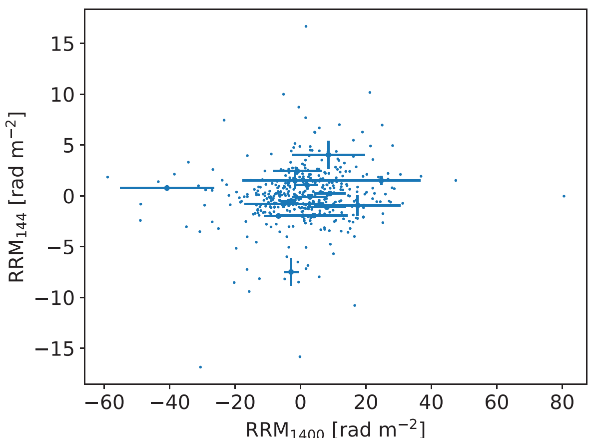

Figure 11. RRM at 144 MHz, RRM_{144}, plotted versus that at 1.4-GHz, RRM_{1400}, for the NVSS/LoTSS sample. Error bars are plotted 1-in-30 sources to avoid too much confusion.

where $RRM_{0,\,f}$ is the average absolute value of the RRM_0 of an individual filament, $N_f(z)$ is taken from equation (22), and A_{RRM} is a constant term that accounts for possible other components of different origin. The resulting fit is shown in Fig. 15, right-hand panel. The fit is a good approximation of the data, making the filament scenario self-consistent again, and the resulting filament $RRM_{0,\,f}$ is

$$RRM_{0,f} = 0.71 \pm 0.07 \text{ rad m}^{-2}, \quad (25)$$

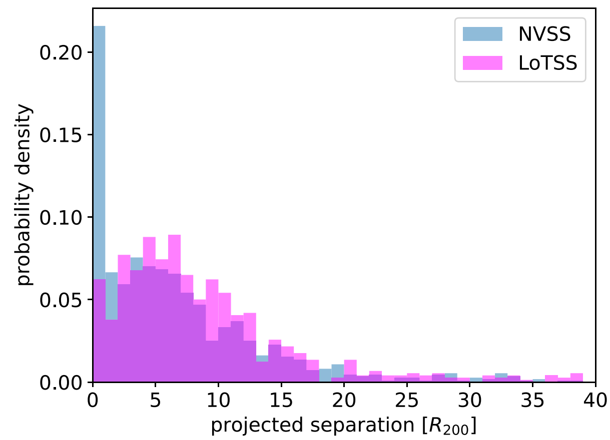

Figure 12. Distribution of the minimum projected separations of sources of the LoTSS and NVSS samples from galaxy clusters. Separations are plotted up to $40 R_{200}$ for viewing reasons; there are 14 more sources of the LoTSS sample and 21 of the NVSS sample beyond that limit.

in broad agreement with the value of 1.5 rad m^{-2} from simulations (Akahori & Ryu 2010) and consistent with previous upper limits (e.g. 3.8 rad m^{-2} by Amaral, Vernstrom & Gaensler 2021). The constant term of the fit is $A_{RRM} = 0.91 \pm 0.18$ rad m^{-2}.

Assuming a typical value for the electron density in filaments[9] of $n_{e,\,f} = 10^{-5}$ cm^{-3} (Akahori & Ryu 2010, 2011; Vazza et al. 2015), a filament width of 3 Mpc (Cautun et al. 2014), and correcting it for the mean inclination of a filament to the line of sight (see Appendix B), we get a filament magnetic field intensity parallel to the line of sight of

$$B_{\parallel,f} = 18.6 \pm 1.9 \text{ nG}, \quad (26)$$

and a filament total magnetic field of

$$B_f = \sqrt{3}\, B_{\parallel,f} = 32.3 \pm 3.2 \text{ nG}, \quad (27)$$

assuming no dependence on z of n_e and the magnetic field B. This is in agreement with Vernstrom et al. (2021) who found a magnetic field intensity per filament of $30 \leq B_f \leq 60$ nG using synchrotron emission stacking. It is also consistent with previous cosmic web magnetic field upper limits or estimates from simulations. Vernstrom et al. (2017) and Brown et al. (2017) found upper limits of 30–200 nG from cross-correlating synchrotron emission with the large-scale structure distribution, Vacca et al. (2018) estimated fields of 10–50 nG from simulations constrained by observations, Vernstrom et al.

[9] $n_{e,\,f}$ is estimated at $z = 0.7$ that in terms of comoving distance is mid-way out to $z = 2$, the range spanned by our data set.

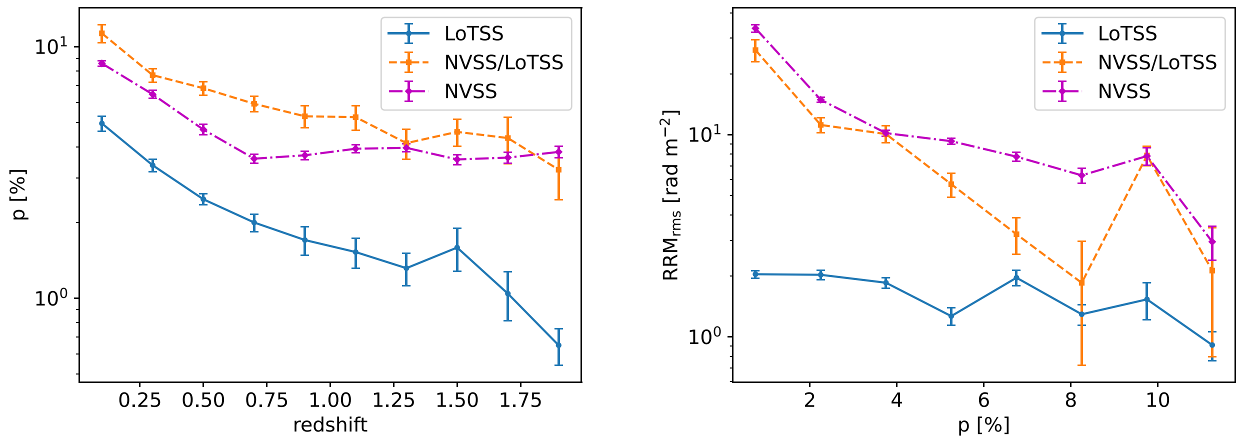

Figure 13. Left-hand panel: mean of fractional polarization p as a function of z for all the samples used in this paper (see the legend). Right-hand panel: RRM deviation (RRM$_{\rm rms}$) as a function of p for all the samples used in this paper (see the legend).

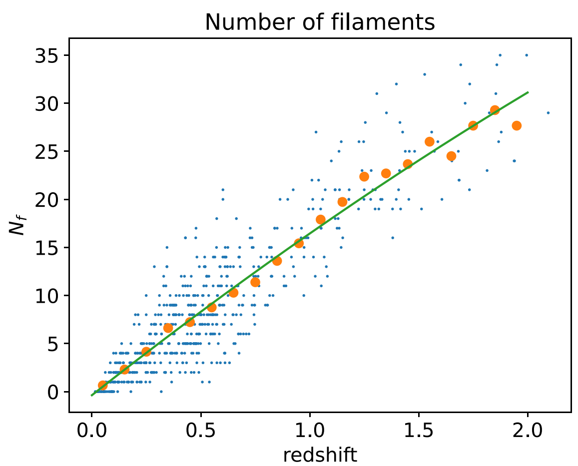

Figure 14. The number of filaments $N_{\rm f}$ versus redshift of each source of the LoTSS sample that falls into the field covered by the filaments catalogues (dots). The best quadratic fit (solid line) and the mean in redshift bins (circles) are also reported.

(2019) estimated an upper limit of 40 nG with RMs of extragalactic source pairs, Amaral et al. (2021) found an upper limit of 50-nG cross-correlating RMs with the galaxy distribution, O'Sullivan et al. (2019) found an upper limit of 250 nG from a differential number of filaments in the foreground of two lobes of a radio galaxy, and Locatelli et al. (2021) estimated an upper limit of 250 nG based on simulations constrained by non-detections.

Our estimate is also in agreement with models based on primordial magnetic fields amplified by astrophysical source seeding, which predict fields of a few tens of nG in filaments, in contrast to a few nG for models based on only primordial magnetic fields grown by MHD processes (e.g. Vazza et al. 2015; Arámburo-García et al. 2021). In principle, models based only on primordial magnetic fields can reach the measured amplitudes but only in the cases that the primordial seed field is at the top of the current upper limits (Vazza et al. 2017). In the more general case, a boost by astrophysical source seeding is required (e.g. Vazza et al. 2015, 2017).

Our result of the detection of a filament RRM$_0$ supports the presence of a baryonic Warm-Hot Ionized Medium (WHIM) in filaments, that cosmological simulations predict to contain some 50 per cent of the cosmic baryons.

We repeated the analysis fitting the RRMs measured in redshift bins with equal number of sources obtaining consistent results (see Appendix C).

An estimate of the turbulent component of the magnetic field of a filament, assuming a Gaussian distribution, can be derived from $\sigma_{\rm RRM_0,f}$ and the Burn Law (Burn 1966; Tribble 1991; Felten 1996; Sokoloff et al. 1998; Enßlin & Vogt 2003; Murgia et al. 2004) with

$$\sigma_{\rm RRM_0,f} = 0.812\, n_{\rm e}\, \sigma_{B_\parallel,\rm f}\, \sqrt{l\, \lambda_B}, \tag{28}$$

$$B_{\rm turb,f} = 2\sqrt{2/\pi}\, \sigma_{B_\parallel,\rm f}, \tag{29}$$

where $B_{\rm turb,\,f}$ and $\sigma_{B_\parallel,\rm f}$ are the mean turbulent magnetic field intensity and the dispersion of its component parallel to the line of sight, l is the radiation's path-length through the filament, and λ_B is the coherence scale of the magnetic field. The latter is expected to be a few 100 h^{-1} kpc (Akahori & Ryu 2010) and we assume it to range within $0.4 < \lambda_B < 1.0$ Mpc. Assuming for the other terms the same values we used to estimate $B_{\rm f}$, we find $3.5 \lesssim B_{\rm turb,\,f} \lesssim 5.5$ nG. This is small compared to $B_{\rm f}$ and so we conclude that the turbulent component is subdominant.

4.4 Local environment

The other option is an origin of RRM and p local to the source for the 144-MHz data. The following considerations can be drawn from the analysis conducted in Section 4.2:

(i) The behaviour with redshift of p at 144 MHz is still compatible with a local origin. The flat behaviour of RRM with p instead disfavours it, because higher RRM values should be accompanied by stronger depolarization, as the 1.4-GHz data show.

(ii) If the origin occurs local to the source it is usually in the medium surrounding it (e.g. Laing et al. 2008) and increasing depolarization (i.e. decreasing p) might be related to larger turbulence at high redshift (equation (20)). The observed sources are in low-density environments far from galaxy clusters, as we have shown, and thus have to be field or group galaxies that can be in a less relaxed state at high redshift than at present with higher turbulence. This can explain the behaviour at 1.4 GHz (see also Berger et al. 2021), but it would cause total depolarization at 144 MHz, which is not what we observe.

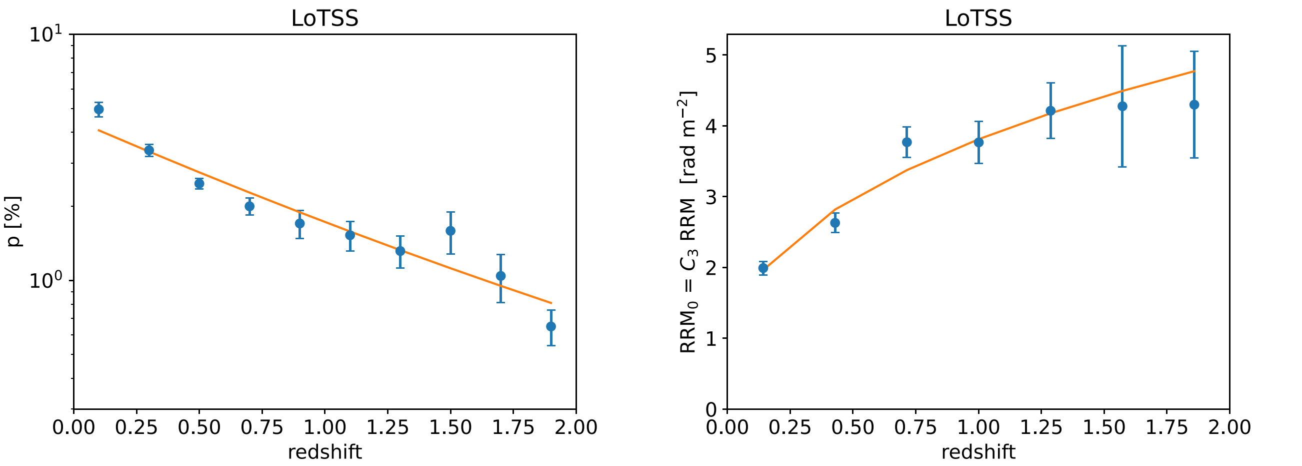

Figure 15. Left-hand panel: polarization fraction p versus redshift of the LoTSS sample (circles) and best fit of the function of equation (21) (solid line). Right-hand panel: RRM_0 as a function of redshift of the LoTSS sample corrected for model C_3 (circles) and best fit of the function of equation (24) (solid line).

We conclude that our data disfavour a local origin being the dominant factor for both the RRM and p observed at 144 MHz, while it most likely is the dominant factor for the 1.4-GHz data (see Section 4.2).

5 CONCLUSIONS

We have analysed the LoTSS DR2 RM Catalogue containing RMs measured at 144 MHz, and in particular a subset of sources with a spectroscopic redshift and above a Galactic latitude cut of $|b| = 25^\circ$, to study the behaviour with redshift of polarization quantities of extragalactic sources in low-density environments in the range $0 < z < 2$. After subtracting the Galactic RM contribution and producing a catalogue of RRM, we measured the behaviour with redshift of the RRM rms deviation and fractional polarization p. We also measured $\langle \mathrm{RRM}^2 \rangle^{1/2}$ as a function of p. We repeated the same analysis for NVSS RMs of sources in the LoTSS sample, to investigate the behaviour of RRM and p measured at 1.4 GHz of the same sample from low-density environments.

Our main findings are as follows:

(i) At 144 MHz, the RRM rms is flat with redshift out to $z = 2$. Once the redshift correction is applied, the rest frequency RRM_0 rms increases with redshift at a high confidence level for all of the correction models we considered, showing a clear evolution with redshift. At 1.4 GHz, the RRM shows a hint of an increase with redshift and RRM_0 increases with z at a high confidence level.

(ii) At 144 MHz, the fractional polarization is anticorrelated with redshift, at $z = 1.9$ it is ∼1/8th of that at $z = 0.1$, showing an evolution with redshift at a high confidence level. Also at 1.4 GHz, p is anticorrelated with redshift at a high confidence level, even though at a lower rate than at 144 MHz (at the high-z end, it is ∼1/3rd of that at the low-z end).

(iii) The RRM rms is flat with p at 144 MHz and no increase of RRM at low p is observed. At 1.4 GHz, instead, RRM rms decreases with p, indicating that sources with a higher RRM are more depolarized.

These findings and our analysis lead us to the following main results:

(i) There is a clear evolution with redshift of p and the rest-frame RRM_0 for the physically motivated redshift correction models we considered.

(ii) Polarized sources at 144 MHz reside far from galaxy clusters with a peak at $\sim 5R_{200}$, confirming they are in low-density environments. The general 1.4-GHz population is closer to clusters, instead, with a substantial fraction within cluster boundaries.

(iii) The RRM and $p(z)$ have a different origin at 144 MHz and 1.4 GHz. Depolarization at 1.4 GHz is not mainly due to the radiation travelling through the IGM on large scales and a local origin is favoured for the RRM and depolarization at this frequency. A passage through filaments of the cosmic web is favoured as the origin of the RRM and $p(z)$ at 144 MHz. The depolarization with z, the flat behaviour of the RRM with z and p, and the fit of p and RRM_0 to that expected by the number of filaments along the line of sight are all consistent with such an origin.

(iv) If we attribute the total RRM and $p(z)$ to cosmic web filaments, we estimate an average RM for an individual filament of $\mathrm{RRM}_{0,\mathrm{f}} = 0.71 \pm 0.07$ rad m^{-2}, and an average magnetic field per filament of $B_\mathrm{f} = 32 \pm 3$ nG, assuming no dependence on z of n_e and B. This value favours models where the field in filaments is amplified by astrophysical source seeding in contrast with models solely based on the growth of primordial magnetic fields.

(v) The detection of a filament RRM_0 supports the presence of a diffuse WHIM in cosmic filaments that were predicted to contain ∼50 per cent of the cosmic baryons.

(vi) We also estimate, for the first time, an average turbulence in each filament of $\sigma_{\mathrm{RRM}_{0,\mathrm{f}}} = 0.0389 \pm 0.0010$ rad m^{-2}. We use it to estimate the turbulent component of the magnetic field in filaments and find that it is subdominant.

With this work we have applied RMs measured at low radio frequencies to detect and measure magnetic fields in cosmic web filaments. We have several hints that the bulk of what we observe at 144 MHz is generated in the IGM, while at 1.4 GHz the observations are dominated by the local source environment. Our estimate for the magnetic field in filaments is in agreement with that found using an independent method based on synchrotron emission stacking (Vernstrom et al. 2021), indicating that these are complementary and effective methods to investigate the cosmic web magnetism. This work shows the importance of low-frequency observations and the availability of sources with measured redshifts to investigate the magnetism in the cosmic web and its evolution with cosmic time. It also shows the importance of having RM measurements at different frequencies to discriminate their origin.

This is an important first step. Several new advances can be achieved in future work. Modelling of the behaviour with z of n_e and B_f can improve our estimate of the filament magnetic field and turbulence, and possibly estimate their evolution with redshift. Larger samples will improve the redshift resolution and bin sensitivity, which will give a more detailed view of the evolution with redshift and extend it to higher redshifts. It will also allow separation into different source populations and investigations of their impact and their own evolution. A first step will be achieved by completing the LoTSS survey and a further leap can be made with a polarization survey carried out with SKA1-LOW (Braun et al. 2019). Comparing results at different frequencies has been essential to the determination of where the RRM is originating. Combining LoTSS, ASKAP-POSSUM (Gaensler et al. 2010), and APERTIF (Berger et al. 2021) data, and in the future, those of the surveys of SKA1–LOW and SKA1–MID (Braun et al. 2019), will help establish more firmly the RRM origin at several frequencies and at what frequency the IGM component starts to prevail. The same surveys can also be used to improve the separation of the extragalactic and Galactic RM components (Hutschenreuter et al. 2022), which is needed to improve the overall precision of the RRM estimates.

ACKNOWLEDGEMENTS

This work has been conducted within the LOFAR Magnetism Key Science Project[10] (MKSP). This work has made use of LoTSS DR2 data. VV acknowledges support from INAF mainstream project 'Galaxy Clusters Science with LOFAR' 1.05.01.86.05. AMS gratefully acknowledges support from the Alan Turing Institute, grant reference EP/V030302/1. CS acknowledges support from the MIUR grant FARE 'SMS'. LOFAR (van Haarlem et al. 2013) is the Low Frequency Array designed and constructed by ASTRON. It has observing, data processing, and data storage facilities in several countries, which are owned by various parties (each with their own funding sources), and which are collectively operated by the ILT foundation under a joint scientific policy. The ILT resources have benefited from the following recent major funding sources: CNRS-INSU, Observatoire de Paris, and Université d'Orléans, France; BMBF, MIWF-NRW, MPG, Germany; Science Foundation Ireland (SFI), Department of Business, Enterprise and Innovation (DBEI), Ireland; NWO, The Netherlands; The Science and Technology Facilities Council, UK; Ministry of Science and Higher Education, Poland; and The Istituto Nazionale di Astrofisica (INAF), Italy. LoTSS made use of the Dutch national e-infrastructure with support of the SURF Cooperative (e-infra 180169) and the LOFAR e-infra group. The Jülich LOFAR Long Term Archive and the German LOFAR network are both coordinated and operated by the Jülich Supercomputing Centre (JSC), and computing resources on the supercomputer JUWELS at JSC were provided by the Gauss Centre for Supercomputing e.V. (grant CHTB00) through the John von Neumann Institute for Computing (NIC). LoTSS made use of the University of Hertfordshire high-performance computing facility and the LOFAR-UK computing facility located at the University of Hertfordshire and supported by STFC [ST/P000096/1], and of the Italian LOFAR IT computing infrastructure supported and operated by INAF, and by the Physics Department of Turin University (under an agreement with Consorzio Interuniversitario per la Fisica Spaziale) at the C3S Supercomputing Centre, Italy. This work made use of the PYTHON packages ASTROPY (Astropy Collaboration et al. 2013) and MATPLOTLIB (Hunter 2007). Some of the results in this paper have been derived using the HEALPY (Zonca et al. 2019) and HEALPIX[11] (Górski et al. 2005) packages.

DATA AVAILABILITY

The LoTSS DR2 RM catalogue will be publicly released as the paper describing it will be accepted for publication. The Hammond catalogue of NVSS RMs with redshift cross-matches (Hammond et al. 2012), the NVSS RM catalogue (Taylor et al. 2009), the galaxy cluster catalogue (Wen & Han 2015), and the cosmic web filament catalogues (Chen et al. 2016; Carrón Duque et al. 2021) are all available at the websites reported in the papers that describe them.

REFERENCES

Ahumada R., et al., 2020, ApJS, 249, 3
Akahori T., Ryu D., 2010, ApJ, 723, 476
Akahori T., Ryu D., 2011, ApJ, 738, 134
Amaral A. D., Vernstrom T., Gaensler B. M., 2021, MNRAS, 503, 2913
Arámburo-García A., Bondarenko K., Boyarsky A., Nelson D., Pillepich A., Sokolenko A., 2021, MNRAS, 505, 5038
Astropy Collaboration et al., 2013, A&A, 558, A33
Berger A., Adebahr B., Herrera Ruiz N., Wright A. H., Prandoni I., Dettmar R. J., 2021, A&A, 653, A155
Bernet M. L., Miniati F., Lilly S. J., Kronberg P. P., Dessauges-Zavadsky M., 2008, Nature, 454, 302
Braun R., Bonaldi A., Bourke T., Keane E., Wagg J., 2019, preprint (arXiv:1912.12699)
Brentjens M. A., de Bruyn A. G., 2005, A&A, 441, 1217
Brown S. et al., 2017, MNRAS, 468, 4246
Burn B. J., 1966, MNRAS, 133, 67
Carrón Duque J., Migliaccio M., Marinucci D., Vittorio N., 2021, preprint (arXiv:2106.05253)
Cautun M., van de Weygaert R., Jones B. J. T., Frenk C. S., 2014, MNRAS, 441, 2923
Chen Y.-C., Ho S., Brinkmann J., Freeman P. E., Genovese C. R., Schneider D. P., Wasserman L., 2016, MNRAS, 461, 3896
Chen Y.-C., Ho S., Freeman P. E., Genovese C. R., Wasserman L., 2015, MNRAS, 454, 1140
Enßlin T. A., Vogt C., 2003, A&A, 401, 835
Ettori S., Balestra I., 2009, A&A, 496, 343
Felten J. E., 1996, in Trimble V., Reisenegger A., eds, ASP Conf. Ser. Vol. 88, Clusters, Lensing, and the Future of the Universe. Astron. Soc. Pac., San Francisco, p. 271
Fujimoto M., Kawabata K., Sofue Y., 1971, Prog. Theo. Phys. Suppl., 49, 181
Gaensler B. M., Landecker T. L., Taylor A. R., POSSUM Collaboration, 2010, AAS Meeting Abstracts, 215, 470.13
Gheller C., Vazza F., Favre J., Brüggen M., 2015, MNRAS, 453, 1164
Górski K. M., Hivon E., Banday A. J., Wandelt B. D., Hansen F. K., Reinecke M., Bartelmann M., 2005, ApJ, 622, 759
Govoni F. et al., 2019, Science, 364, 981
Hammond A. M., Robishaw T., Gaensler B. M., 2012, preprint (arXiv:1209.1438)
Heald G. et al., 2020, Galaxies, 8, 53
Hunter J. D., 2007, Comput. Sci. Eng., 9, 90
Hutschenreuter S. et al., 2022, A&A, 657, A43
Kronberg P. P., Bernet M. L., Miniati F., Lilly S. J., Short M. B., Higdon D. M., 2008, ApJ, 676, 70

[10] https://lofar-mksp.org/.

[11] http://healpix.sf.net.

Kronberg P. P., Perry J. J., 1982, ApJ, 263, 518
Kronberg P. P., Reinhardt M., Simard-Normandin M., 1977, A&A, 61, 771
Laing R. A., Bridle A. H., Parma P., Murgia M., 2008, MNRAS, 391, 521
Lamee M., Rudnick L., Farnes J. S., Carretti E., Gaensler B. M., Haverkorn M., Poppi S., 2016, ApJ, 829, 5
Locatelli N., Vazza F., Bonafede A., Banfi S., Bernardi G., Gheller C., Botteon A., Shimwell T., 2021, A&A, 652, A80
Massaro E., Maselli A., Leto C., Marchegiani P., Perri M., Giommi P., Piranomonte S., 2015, ApSS, 357, 75
Murgia M., Govoni F., Feretti L., Giovannini G., Dallacasa D., Fanti R., Taylor G. B., Dolag K., 2004, A&A, 424, 429
O'Sullivan S. P. et al., 2019, A&A, 622, A16
O'Sullivan S. P. et al., 2020, MNRAS, 495, 2607
Oppermann N. et al., 2015, A&A, 575, A118
Oren A. L., Wolfe A. M., 1995, ApJ, 445, 624
Planck Collaboration et al., 2020, A&A, 641, A6
Porayko N. K. et al., 2019, MNRAS, 483, 4100
Reinhardt M., 1972, A&A, 19, 104
Riseley C. J. et al., 2020, PASA, 37, e029
Shimwell T. W. et al., 2017, A&A, 598, A104
Shimwell T. W. et al., 2019, A&A, 622, A1
Shimwell T. W., et al., 2022, A&A, 659, A1
Sofue Y., Fujimoto M., Kawabata K., 1979, PASJ, 31, 125
Sokoloff D. D., Bykov A. A., Shukurov A., Berkhuijsen E. M., Beck R., Poezd A. D., 1998, MNRAS, 299, 189
Sotomayor-Beltran C. et al., 2013, A&A, 552, A58
Stuardi C. et al., 2020, A&A, 638, A48
Subramanian K., 2016, Rep. Prog. Phys., 79, 076901
Taylor A. R., Stil J. M., Sunstrum C., 2009, ApJ, 702, 1230
Thomson R. C., Nelson A. H., 1982, MNRAS, 201, 365
Tribble P. C., 1991, MNRAS, 253, 147
Vacca V. et al., 2018, MNRAS, 479, 776
van Haarlem M. P. et al., 2013, A&A, 556, A2
Vazza F., Brüggen M., Gheller C., Hackstein S., Wittor D., Hinz P. M., 2017, Class. Quantum Gravity, 34, 234001
Vazza F., Ferrari C., Brüggen M., Bonafede A., Gheller C., Wang P., 2015, A&A, 580, A119
Vernstrom T., Gaensler B. M., Brown S., Lenc E., Norris R. P., 2017, MNRAS, 467, 4914
Vernstrom T., Gaensler B. M., Rudnick L., Andernach H., 2019, ApJ, 878, 92
Vernstrom T., Gaensler B. M., Vacca V., Farnes J. S., Haverkorn M., O'Sullivan S. P., 2018, MNRAS, 475, 1736
Vernstrom T., Heald G., Vazza F., Galvin T. J., West J. L., Locatelli N., Fornengo N., Pinetti E., 2021, MNRAS, 505, 4178
Welter G. L., Perry J. J., Kronberg P. P., 1984, ApJ, 279, 19
Wen Z. L., Han J. L., 2015, ApJ, 807, 178
Wen Z. L., Han J. L., Liu F. S., 2012, ApJS, 199, 34
Xu J., Han J. L., 2022, ApJ, 926, 65
You X. P., Han J. L., Chen Y., 2003, Acta Astron. Sin., 44, 155
Zonca A., Singer L., Lenz D., Reinecke M., Rosset C., Hivon E., Gorski K., 2019, J. Open Source Softw., 4, 1298

APPENDIX A: RRM EVOLUTION WITH REDSHIFT OF THE LOTSS SAMPLE IN REDSHIFT BINS WITH EQUAL NUMBER OF SOURCES

We computed the RRM mean and rms deviation of the LoTSS sample in redshift bins with equal number of sources, 64 each (Fig. A1). The redshift resolution is higher at low z and coarser at high z, so this can give a better view of where the rest-frame RRM_0 starts to increase. The uncorrected RRM is bumpy compared to the case with equal-width bins, but it is still flat with a linear-fit slope of 0.13 ± 0.2. All of the rest-frame-corrected RRM_0 are bumpy, but they show a clear increasing behaviour with z, starting from the low-redshift end. A linear fit (Table A1) shows that the slope is again non-flat at a high confidence level: $\beta/\sigma_\beta = 11.2, 7.2, 5.1$ for the three correction models C_1 to C_3, with Student's t-test p-values of $p_t = 2.4 \times 10^{-8}$, 3.4×10^{-6}, and 1.1×10^{-4}, respectively. That confirms a clear evolution of RRM_0 with z (see also the Spearman tests in Table A1).

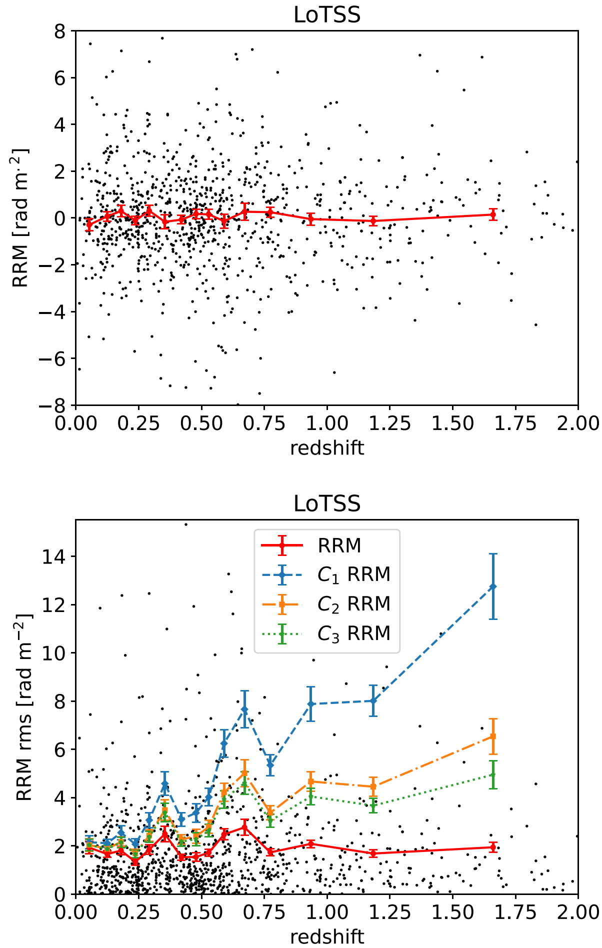

Figure A1. Top panel: as for Fig. 4, top panel, but the RRM mean is in redshift bins with equal number of sources (red solid line). Bottom panel: as for Fig. 4, bottom panel, except the RRM rms deviation is in redshift bins with equal number of sources (red solid line). The number of bins is higher, redshift resolution is finer at low z and coarser at high z. The rest-frame RRM_0 corrected for the redshift effect for the three models C_x are also plotted.

Table A1. As for Table 2, except it is for the case of redshift bins with equal number of sources.

model	α (rad m^{-2})	β (rad m^{-2})	$t = \beta/\sigma_\beta$	p_t	ρ	p_ρ
C_1	1.24 ± 0.42	6.64 ± 0.59	11.2	$2.4\ 10^{-8}$	0.94	$1.4\ 10^{-7}$
C_2	1.65 ± 0.28	2.91 ± 0.40	7.2	$3.4\ 10^{-6}$	0.88	$1.4\ 10^{-5}$
C_3	1.87 ± 0.27	1.97 ± 0.39	5.1	$1.1\ 10^{-4}$	0.87	$2.8\ 10^{-5}$

APPENDIX B: MEAN PATH-LENGTH THROUGH A FILAMENT

The path-length along the line of sight through a filament of width D and inclination θ to the line of sight is

$$l = \frac{D}{\sin\theta}. \tag{B1}$$

The mean path-length averaged over all filament orientations thus is

$$\bar{l} = \frac{1}{4\pi}\int_0^{2\pi} d\varphi \int_0^{\pi} \frac{D}{\sin\theta}\ \sin\theta\, d\theta \tag{B2}$$

$$= \frac{\pi}{2}\, D. \tag{B3}$$

APPENDIX C: FILAMENT MAGNETIC FIELD ESTIMATE WITH REDSHIFT BINS WITH EQUAL-NUMBER OF SOURCES

Following the procedure of Section 4.3, we repeated the estimate of the total magnetic field of individual filaments using the RRM rms measured in redshift bins with equal number of sources (Fig. A1).

The fit of equation (24) to the rest frequency RRM_0 rms is shown in Fig. C1. The resulting filament $\mathrm{RRM}_{0,\,\mathrm{f}}$ is

$$\mathrm{RRM}_{0,\mathrm{f}} = 0.64 \pm 0.07\ \mathrm{rad\,m^{-2}}. \tag{C1}$$

Making the same assumptions as for the main text we get a filament total magnetic field of

$$B_\mathrm{f} = 29 \pm 3\,\mathrm{nG}. \tag{C2}$$

This is consistent with the result of Section 4.3, within the errors.

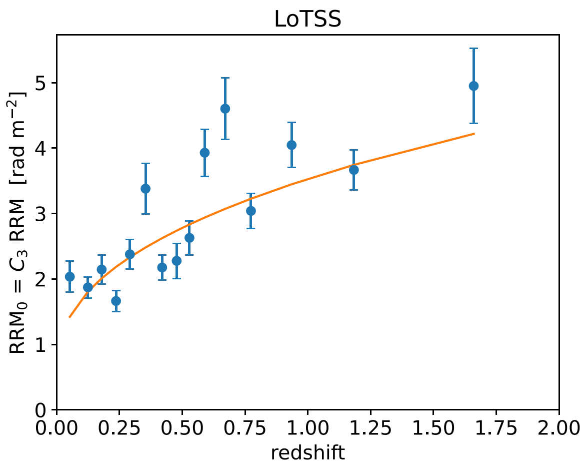

Figure C1. RRM_0 as a function of redshift of the LoTSS sample corrected for model C_3 (circles) in the case of redshift bins with equal number of sources and best fit of the function of equation (24) (solid line).

This paper has been typeset from a TEX/LATEX file prepared by the author.